The Source of Saturn's G Ring
Matthew M. Hedman, *et al.*
Science **317**, 653 (2007);
DOI: 10.1126/science.1143964

Science (print ISSN 0036-8075; online ISSN 1095-9203) is published weekly, except the last week in December, by the American Association for the Advancement of Science, 1200 New York Avenue NW, Washington, DC 20005. Copyright 2007 by the American Association for the Advancement of Science; all rights reserved. The title *Science* is a registered trademark of AAAS.

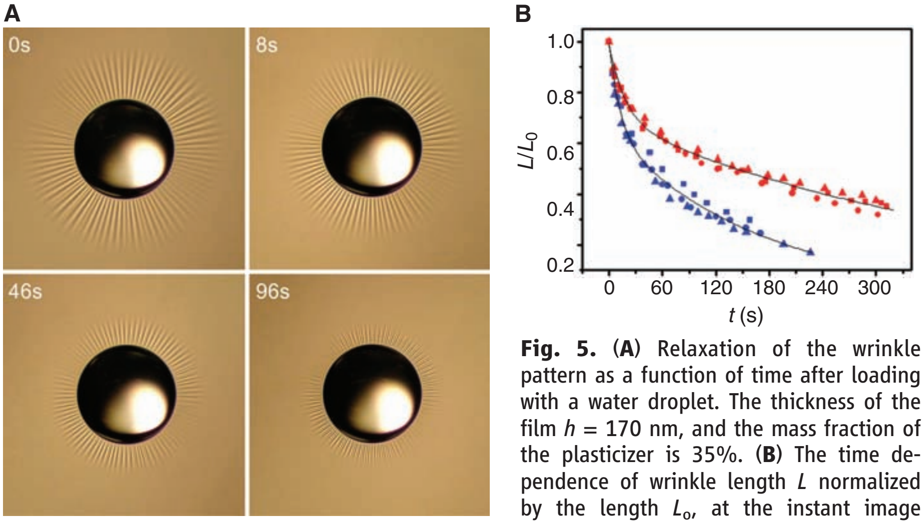

Fig. 5. (**A**) Relaxation of the wrinkle pattern as a function of time after loading with a water droplet. The thickness of the film $h = 170$ nm, and the mass fraction of the plasticizer is 35%. (**B**) The time dependence of wrinkle length L normalized by the length L_o, at the instant image capture commenced. Data are shown for plasticizer mass fractions of 35% (blue symbols) and 32% (red symbols). The plot symbols differentiate experimental runs, showing reproducibility of the time dependence. Solid lines show fits to a stretched exponential: $L(t)/L_o = \exp[-(t/\tau)^\beta]$.

(Fig. 4B) with our x-ray reflectivity measurements of h. Thus, measurements of both modulus and thickness can be achieved by a wrinkling assay with comparable or higher precision, and with very basic instrumentation, when compared to the other techniques on display in Fig. 4, each of which involves sophisticated equipment and yields only one of E or h.

Further, in contrast to the few other methods available for measuring the modulus of extremely thin films, such as nano-indentation (*13*) or stress-induced buckling (*12*), the measurement is performed with the film on a fluid surface, rather than mounted on a solid substrate. This allows the possibility for the film to relax internal mechanical stresses that can develop either in the spin-coating process or during transfer to a solid substrate. Apart from the ability to make measurements on a state that is not pre-stressed, this opens the possibility of measuring bulk relaxational properties of the film without concerns about pinning to a substrate. In Fig. 5A, we show a sequence of images visualizing the time-dependent relaxation of the wrinkle pattern formed by a capillary load. At increasing time, the wrinkles smoothly reduce in length and finally disappear. The strains that develop in response to the capillary load (*14*) can relax due to the viscoelastic response of the PS charged with a large mass fraction of plasticizer. In Fig. 5B, we show the time dependence of wrinkle length, $L(t)$, for two sets of films with different plasticizer mass fraction, x. $L(t)$ can be fit with a stretched exponential function $L_o \exp[-(t/\tau)^\beta]$, where τ decreases with increasing plasticizer concentration, and $\beta = 0.50 \pm 0.02$, typical of polymer viscoelastic response near the glass transition (*13*, *15*).

Thus, capillary-driven wrinkle formation can be used as the basis for a metrology of both the elastic modulus and the thickness of ultrathin films by means of a very elementary apparatus—a low-magnification microscope and a dish of fluid. This simple technique can also be used to study dynamical relaxation phenomena in ultrathin films.

References and Notes

1. E. Cerda, K. Ravi-Chander, L. Mahadevan, *Nature* **419**, 579 (2002).
2. E. Cerda, L. Mahadevan, *Phys. Rev. Lett.* **90**, 074302 (2003).
3. K. Efimenko *et al.*, *Nat. Mater.* **4**, 293 (2005).
4. J. Genzer, J. Groenewold, *Soft Matter* **2**, 310 (2006).
5. E. Cerda, *J. Biomech.* **38**, 1598 (2005).
6. T. P. Russell, *Mat Sci. Rep.* **5**, 171 (1990).
7. Supporting material is available on *Science* Online.
8. J.-C. Geminard, R. Bernal, F. Melo, *Eur. Phys. J. E* **15**, 117 (2004).
9. L. D. Landau, E. M. Lifshitz, *Theory of Elasticity, Course of Theoretical Physics* (Butterworth-Heinemann, India, ed. 3, 1986), vol. 7.
10. S. Timoshenko, J. Goodier, *Theory of Elasticity* (McGraw-Hill, New York, ed. 3, 1987).
11. J. Brandrup, E. H. Immergut, Polymer Handbook (Wiley, New York, ed. 3, 1989).
12. C. M. Stafford *et al.*, *Nat. Mater.* **3**, 545 (2004).
13. K. Miyake, N. Satomi, S. Sasaki, *Appl. Phys. Lett.* **89**, 031925 (2006).
14. H. Bodiguel, C. Fretigny, *Eur. Phys. J. E* **19**, 185 (2006).
15. N. G. McCrum, B. E. Reed, G. Williams, *Anelastic and Dielectric Effects in Polymeric Solids* (Wiley, London, 1967).
16. We acknowledge support from the Center for University of Massachusetts–Industry Cooperative Research Program (J.H.); the NSF–supported Materials Research Science and Engineering Center on Polymers at the University of Massachusetts (W.H.J.); the U.S. Department of Energy, Office of Basic Energy Science, through DE-FG-0296 ER45612 (T.P.R.); and the NSF through contracts NSF-DMR 0606216 (N.M.) and NSF-CBET-0609107 (T.S.E., T.P.R., and N.M.). We gratefully acknowledge useful conversations with A. D. Dinsmore.

Supporting Online Material

www.sciencemag.org/cgi/content/full/317/5838/650/DC1
Materials and Methods
Figs. S1 and S2

3 May 2007; accepted 15 June 2007
10.1126/science.1144616

The Source of Saturn's G Ring

Matthew M. Hedman,[1]* Joseph A. Burns,[1,2] Matthew S. Tiscareno,[1] Carolyn C. Porco,[3] Geraint H. Jones,[4,5] Elias Roussos,[4] Norbert Krupp,[4] Chris Paranicas,[6] Sascha Kempf[7]

The origin of Saturn's narrow G ring has been unclear. We show that it contains a bright arc located 167,495.6 ± 1.3 km from Saturn's center. This longitudinally localized material is trapped in a 7:6 corotation eccentricity resonance with the satellite Mimas. The cameras aboard the Cassini spacecraft mainly observe small (1 to 10 micrometers) dust grains in this region, but a sharp decrease in the flux of energetic electrons measured near this arc requires that it also contain larger (centimeter- to meter-sized) bodies whose total mass is equivalent to that of a ~100-meter-wide ice-rich moonlet. Collisions into these bodies may generate dust, which subsequently drifts outward to populate the rest of the G ring. Thus, the entire G ring could be derived from an arc of debris held in a resonance with Mimas.

The G ring is unique among Saturn's major rings in that, before the arrival of the Cassini spacecraft, there was no obvious explanation for its location. The dust-sized particles that dominate this ring's optical properties should erode quickly in Saturn's magnetosphere, yet there was no direct evidence for larger source bodies that could replenish the dust and no clear explanation for the concentration of such bodies in this one region (*1*–*5*). Unlike the E and F rings, which are closely associated with satellites that could either directly supply material to the ring (Enceladus) or potentially confine the ring particles into a narrow region (Prometheus and Pandora), the G ring is located 168,000 km from Saturn's center, over 15,000 km from the nearest known satellite. However, using data from the remote-sensing and in situ instruments onboard

---

[1] Department of Astronomy, Cornell University, Ithaca, NY 14853, USA. [2] Department of Theoretical and Applied Mechanics, Cornell University, Ithaca, NY 14853, USA. [3] Cassini Imaging Central Laboratory for Operations, Space Science Institute, Boulder, CO 94043, USA. [4] Max Planck Institut für Sonnensystemforschung, Katlenburg-Lindau 37191, Germany. [5] Mullard Space Science Laboratory, Department of Space and Climate Physics, University College London, Holmbury St. Mary, Dorking, Surrey RH5 6NT, UK. [6] Applied Physics Laboratory, Johns Hopkins University, Laurel, MD 20723, USA. [7] Max Planck Institut für Kernphysik, Saupfercheckweg 1, 69117 Heidelberg, Germany.

*To whom correspondence should be addressed. E-mail: mmhedman@astro.cornell.edu

the Cassini spacecraft, we have identified a structure that may be the source of this mysterious ring.

The Imaging Science Subsystem (ISS) onboard the Cassini spacecraft (*6*) obtained its most comprehensive view of the G ring on 19 September 2006, revealing a localized brightness enhancement near the ring's inner edge around 167,500 km from Saturn's center (Fig. 1). This feature extends over ~60° in longitude and has a radial full width at half maximum (FWHM) of ~250 km, much less than the ~6000-km radial extent of the entire G ring (see Figs. 2, 3).

At least five other image sequences obtained during the first 2 years of the Cassini mission observed this arc [Fig. 3 and supporting online material (SOM)], demonstrating that it is a persistent feature of the ring. Based on these measurements, we estimate that the arc's mean orbital motion is 445.475° ± 0.007°/day (period = 0.808126 ± 0.000013 day), where the uncertainty permits a 5° shift in the arc's position over 2 years. Given current measurements of Saturn's gravitational potential (*7*), this mean motion corresponds to an orbital semimajor axis a = 167,495.6 ± 1.3 km.

The arc's mean motion is extremely close to the Mimas 7:6 corotation eccentricity resonance (CER) at 445.484°/day (a = 167,493.4 km) (*8*). Corotation resonances have been invoked previously to explain arcs in Neptune's rings (*9*–*11*). In our case, perturbations from Mimas can constrain particles to librate around any of six stable longitudes λ where the resonant argument $\varphi_{CER} = 7\lambda_M - 6\lambda - {,}_M$ equals 180° (λ_M and ${,}_M$ are the satellite Mimas' mean longitude and pericenter, respectively). An ensemble of such trapped particles could produce a longitudinally confined structure ~60° wide like the observed arc. Furthermore, throughout the first 2 years of the Cassini mission, the arc's peak has remained near one of the six stable points with $|\Delta\varphi_{CER}| < 40°$.

To verify this model, we conducted numerical simulations of 3830 massless test particles initially placed within 20 km of the Mimas 7:6 CER (see SOM). Most simulated particles (2820) were clearly trapped in the CER (with $|\Delta\varphi_{CER}| <$ 150°) over our 80-year integration. The dominant libration period was 1273 ± 3 days, significantly longer than the interval covered by the currently available observations. The marginally significant (0.009° ± 0.007°/day) drift in the arc's observed position relative to the stable points could therefore be part of a libration cycle. The mean epicyclic eccentricity of the simulated particles ranges from 0.0001 to 0.001 depending on $\Delta\varphi_{CER}$, consistent with the arc's ~250-km radial width (equivalent to an eccentricity ~ 0.0007).

Besides scattering light, the G ring and its arc also absorb magnetospheric particles, leaving detectable imprints on the local plasma environment. In fact, before Voyager took its first pictures of the G ring, Pioneer 11 detected subtle but persistent longitudinally averaged decreases (macrosignatures) in high-energy (<10 MeV) proton fluxes in this region (*12*). More recently, the Magnetospheric Imaging Instrument's Low Energy Magnetospheric Measurements System (LEMMS) onboard the Cassini spacecraft (which measures the flux of electrons with energies between 20 keV and 40 MeV) (*13*) has detected microsignatures (localized depletions in the electron flux) around the G ring. At ~12:13 universal time (UT) on 5 September 2005, this instrument observed an unprecedented ~50% decrease in electron flux while Cassini was moving outbound from Saturn (Fig. 2), and a candidate signature was detected inbound at ~11:58 UT. Two previous passages near the G ring did not show a strong absorption (see SOM).

Using the arc's orbital period determined above, Cassini's location relative to the arc can be plotted for all three passages near the G ring (Fig. 4). The 5 September 2005 passage was much closer to the arc than the others and, when mapped to the equatorial plane, the outbound microsignature's radial profile was 250 km wide, consistent with the arc's inferred density profile (Fig. 2). The absorption signature is most apparent in the LEMMS channels that measure mega–electron volt electrons. Electrons with energies around 1 MeV near the G ring have net azimuthal speeds close to the Keplerian orbital rate, allowing for the formation of very deep absorption signatures. These data strongly suggest that material associated with the arc caused the deep absorption.

The inferred position of the outbound microsignature in Saturn's equatorial plane is displaced roughly 3000 km exterior to the arc (Fig. 2), but this is not too surprising because similar displacements are observed in the signatures of Saturn's small and mid-sized satellites (*14*, *15*). Depletions in charged particles will drift and fill in at different rates, depending on the electrons' energies and the pitch angles of the electrons' trajectories around the magnetic field lines, so the

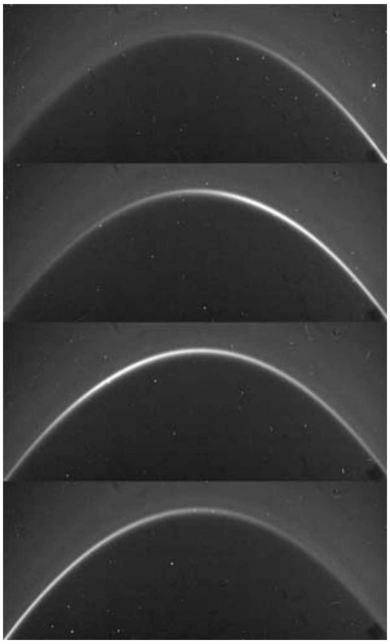

Fig. 1. Images of the G ring arc obtained on 19 September 2006 at 12:37, 13:11, 13:44, and 14:18 UTC from top to bottom. A bright arc moves from right to left through the field of view.

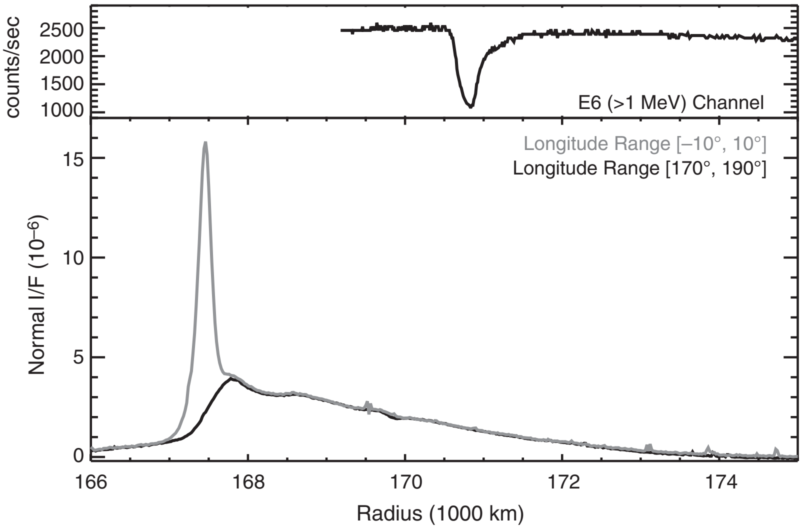

Fig. 2. (**Top**) The charged-particle flux detected by LEMMS channel E6 (*13*, *15*) during Cassini's passage over the arc region on 5 September 2005. The radial scale here corresponds to the equatorial distance of the unperturbed magnetic field lines that thread Cassini at the time of the observation. (**Bottom**) Average (offset-subtracted) radial brightness profiles of the G ring at different longitudes relative to the arc's peak based on data from 19 September 2006. The profiles through the arc (gray) and elsewhere (black) are essentially identical outside 168,000 km, whereas the arc is the sharp peak at 167,500 km in the gray profile. The absorption feature's radial width is comparable to the visible arc's. The 3000-km radial offset between the two signatures may be caused by magnetospheric effects (see SOM).

microsignature could be displaced by larger-scale magnetospheric processes or through a deformation of the local magnetic field by the arc itself.

For a given set of electron pitch angles (near 30° during this observation) and energies (which determine the electron's drift rate relative to the arc), and assuming absorbers composed primarily of water ice, the total arc mass can be estimated from the magnitude of the LEMMS absorption (*16*). For energies between 1 and 10 MeV, the observed depletion implies a total mass between 10^8 and 10^{10} kg (see SOM). If all this material were gathered into a single body, that object would be roughly 100 m across. Because the gyroradii of 1-MeV electrons are on the order of a few kilometers here, the absorption signature's 250-km width indicates that this mass is not in a single body but is instead distributed among multiple objects.

The arc observed in imaging data has a peak normalized reflectance (or normal *I*/*F*, see SOM) that increases from 10^{-6} to 10^{-5} between phase angles of 90° and 165°. Such strong forward scattering implies that the cameras mostly see dust grains 1 to 10 μm across (*17*). The *I*/*F* values indicate that the normal optical depth in this dust is ~10^{-5}, implying that the entire arc contains between 10^5 and 10^6 kg of dust, which is much less than the absorbing mass required by the in situ data. The arc must therefore contain a population of larger particles ranging from centimeters to meters across. The size distribution of these larger objects is not strongly constrained, but if we assume for simplicity that the larger bodies in the arc are on average ~1 m across, their total optical depth would only be around 10^{-7}, well below our current optical detection limit and comparable to previous estimates based on Voyager and Pioneer data (*1*). We propose that impact ejecta from these objects supply the dust that forms not only the visible arc but ultimately also the rest of the G ring.

The bulk of the visible G ring lies exterior to the arc, and the radial brightness profile of the outer part of the G ring decays exponentially with a scale length of approximately 3500 km (*18*) (Fig. 2). Curiously, the Cosmic Dust Analyzer's (CDA) High Rate Detector (HRD) onboard the Cassini spacecraft (*19*) recorded an impact with an exceptionally large dust grain at 10:38:25 UT on 5 September 2005, when the spacecraft passed through the ring plane at 176,700 km, near the outermost edge of the visible G ring. Although the exact size of this grain is uncertain, it produced damage that was never observed in laboratory experiments with grains less than 100 μm across, so this grain was probably at least 100 μm in size. We can explain both of these phenomena with a simple model similar to one

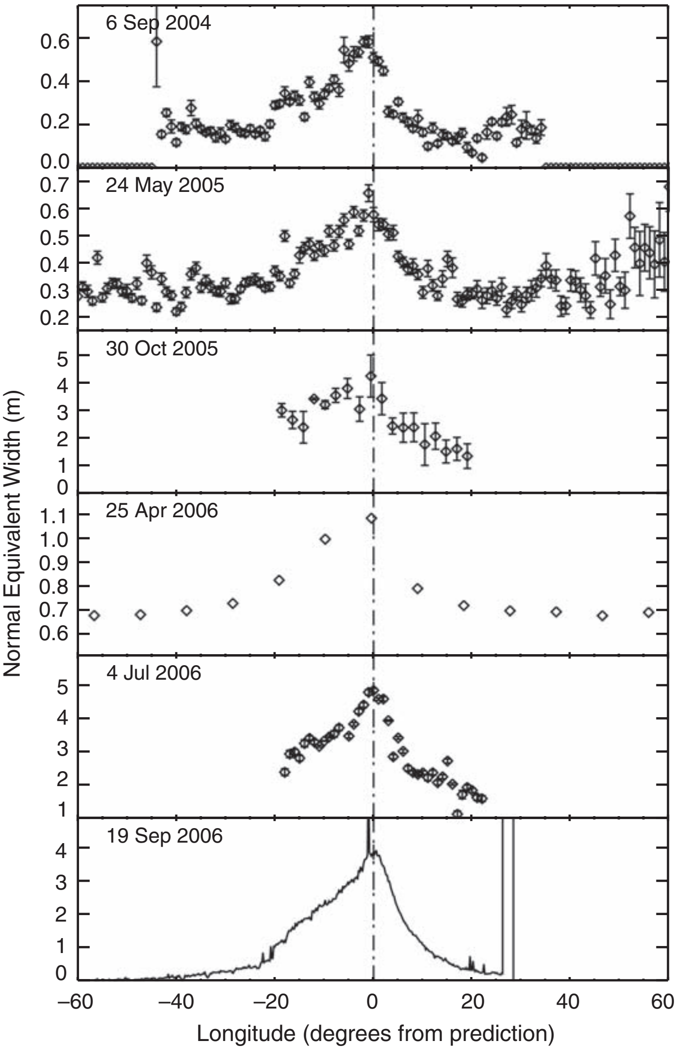

Fig. 3. Six profiles of the G-ring arc's radially integrated brightness (see SOM) versus longitude relative to a coordinate system rotating with a mean motion of 445.475°/day. Errors are based on random noise in the images. These errors are 0.02 and 0.1 m for the 25 April 2006 and 19 September 2006 data, respectively, and so are not plotted. The arc's longitudinal extent is <60°, as expected for a collection of particles trapped in a 7:6 resonance.

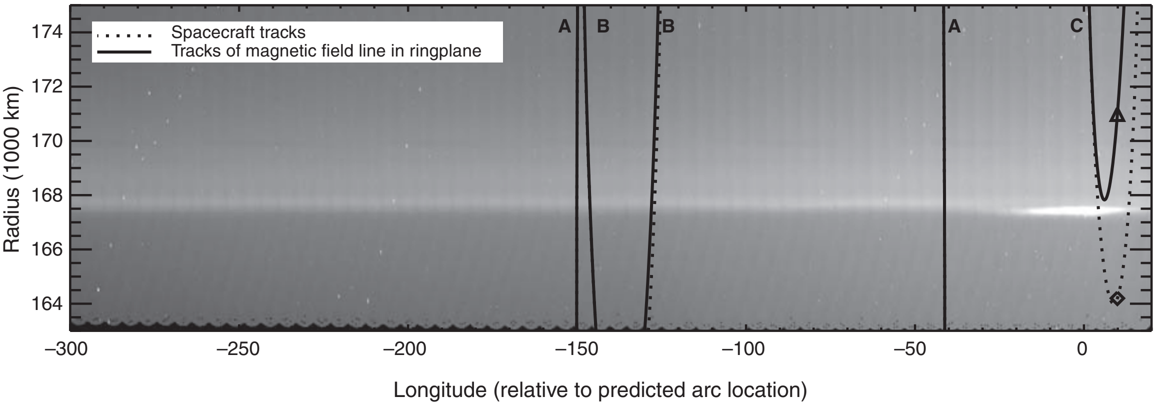

Fig. 4. Correlation between remote-sensing and in situ data. The background image shows the G ring's brightness as a function of radius and longitude measured relative to the arc's center (at 0°). The dotted lines trace Cassini's orbit during its three passages through this region (A = 1 July 2004, B = 14 April 2005, C = 5 September 2005). The solid lines show where an unperturbed magnetic field line threading through the spacecraft would intersect the ring plane during these times. The triangle and diamond mark the time of the strongest absorption detected by LEMMS on 5 September 2005 (Fig. 2).

previously proposed for other dusty rings (*17*, *20*), where small grains released from the arc drift outward under the influence of nongravitational drag forces (such as plasma drag) while they are steadily eroded by collisions with ions, atoms, and smaller grains.

Consider that the visible arc represents dust released from the surfaces of larger bodies by collisions. Although the source bodies are trapped in the Mimas resonance, interactions with Saturn's magnetosphere allow dust to escape this region (*17*). The magnetospheric plasma corotates with the planet's magnetic field (period ~ 0.45 days) (*21*), so its mean motion is much faster than the dust grains' Keplerian orbital motion. Momentum transfer from the plasma therefore causes the dust to drift outward over time. For a particle of mass m located at semimajor axis a and with an orbital velocity v, a drag force F_D will cause a motion $da/dt = a/v(F_D/m)$. In general, F_D is proportional to the particle's surface area whereas m is proportional to its volume, so $da/dt \propto 1/s$, where s is the dust grain's linear size.

As the dust grains drift outward, they will be steadily eroded by collisions with plasma ions, energetic particles, and other small grains. So long as the collisions do not completely shatter the drifting grain (*17*), the mass loss rate will be proportional to the impactor flux times the grain's cross-sectional area, so $dm/dt \propto s^2$ and $ds/dt \propto s^0$. Thus, $ds/da \propto s$. Given that the G ring is narrow ($\delta a/a \sim 0.05$) and assuming that the drag forces and erosion rates do not vary significantly across this region, s should therefore decay exponentially with distance from the source region δa; that is, $s = s_o e^{-\delta a/3D}$, where s_o is the initial particle size, e is the base of natural logarithms, and $3D$ is a scale length determined by the orbital and magnetospheric environments.

The G ring's brightness and optical depth τ at a given δa are proportional to the integral of the particle cross section over the differential particle size distribution at that location [$\tau = \int \pi s^2 n(s,\delta a) ds$]. Assuming that the ring is in a steady state, continuity requires that the number flux of particles of a size s at a distance δa from the arc equal the flux of particles of size s_o released from the arc, which requires that $n(s,\delta a) = n(s_o,0)$ (see SOM). Hence, τ scales like s^3 and the optical depth also decreases exponentially with radial distance from the arc/source, but with a scale length of D instead of $3D$: $\tau = \tau_o e^{-\delta a/D}$. This simple, generic model therefore produces a radial brightness profile with the same basic shape as that observed in the remote-sensing data. Furthermore, the shorter scale length in the optical depth means that although the brightness of the ring at 176,700 km is reduced by over an order of magnitude, individual particle sizes are reduced by only a factor of 2 or 3, so the grain detected by CDA could have been as small as about 200 μm across when it escaped the arc (that is, still small enough to be subject to nongravitational accelerations).

References and Notes

1. M. R. Showalter, J. N. Cuzzi, *Icarus* **103**, 124 (1993).
2. R. Canup, L. W. Esposito, *Icarus* **126**, 28 (1997).
3. H. B. Throop, L. W. Esposito, *Icarus* **131**, 152 (1998).
4. J. J. Lissauer, R. G. French, *Icarus* **146**, 12 (2000).
5. I. dePater, S. C. Martin, M. R. Showalter, *Icarus* **172**, 446 (2004).
6. C. C. Porco *et al.*, *Space Sci. Rev.* **115**, 363 (2004).
7. R. A. Jacobson *et al.*, *Astron. J.* **132**, 2520 (2006).
8. Mimas' 7:6 inner Lindblad resonance also lies nearby at 445.411°/day (a = 167,511 km).
9. P. Goldreich, S. Tremaine, N. Borderies, *Astron. J.* **92**, 490 (1986).
10. C. C. Porco, *Science* **253**, 995 (1991).
11. F. Namouni, C. C. Porco, *Nature* **417**, 45 (2002).
12. J. A. van Allen, *J. Geophys. Res.* **88**, 6911 (1983).
13. S. M. Krimigis *et al.*, *Space Sci. Rev.* **114**, 233 (2004).
14. G. H. Jones *et al.*, *Science* **311**, 1412 (2006).
15. E. Roussos *et al.*, *Icarus*, in press.
16. J. N. Cuzzi, J. A. Burns, *Icarus* **74**, 284 (1988).
17. J. A. Burns, D. P. Hamilton, M. R. Showalter, in *Interplanetary Dust*, E. Grün, B. Gustafson, S. Dermott, H. Fecthig, Eds. (Springer, New York, 2001), pp. 641–725.
18. Slight deviations from an exponential profile occur around 168,200 and 169,800 km. The latter feature shows longitudinal structure and is probably associated with the Mimas 8:7 inner Lindblad resonance.
19. R. Srama *et al.*, *Space Sci. Rev.* **114**, 465 (2004).
20. J. A. Burns, M. R. Showalter, G. E. Morfill, in *Planetary Rings*, R. Greenberg, A. Brahic, Eds. (Univ. of Arizona Press, Tucson, AZ, 1984), pp. 200–272.
21. D. Gurnett *et al.*, *Science* **316**, 442 (2007).
22. We thank the staff at the Space Science Institute, Jet Propulsion Laboratory, and Cornell University for planning and delivering the imaging data, and M. Kusterer of the Johns Hopkins University Applied Physics Laboratory (JHUAPL) for LEMMS data reduction. We also acknowledge the support of the Cassini Project and NASA's Planetary Geology & Geophysics program. MIMI/LEMMS was in part financed by the German Bundesministerium für Bildung und Forschung through the German Aerospace Center (DLR) under contract 50 OH 0103 and by the Max Planck Gesellschaft. The work at JHUAPL was supported by NASA under contract NAS5-97271 with the Johns Hopkins University. G.H.J. was partially supported by the Science and Technology Facilities Council, UK.

18 April 2007; accepted 14 June 2007
10.1126/science.1143964

The FERONIA Receptor-like Kinase Mediates Male-Female Interactions During Pollen Tube Reception

Juan-Miguel Escobar-Restrepo,[1] Norbert Huck,[1] Sharon Kessler,[1] Valeria Gagliardini,[1] Jacqueline Gheyselinck,[1] Wei-Cai Yang,[2] Ueli Grossniklaus[1]*

In flowering plants, signaling between the male pollen tube and the synergid cells of the female gametophyte is required for fertilization. In the *Arabidopsis thaliana* mutant *feronia* (*fer*), fertilization is impaired; the pollen tube fails to arrest and thus continues to grow inside the female gametophyte. *FER* encodes a synergid-expressed, plasma membrane–localized receptor-like kinase. We found that the FER protein accumulates asymmetrically in the synergid membrane at the filiform apparatus. Interspecific crosses using pollen from *Arabidopsis lyrata* and *Cardamine flexuosa* on *A. thaliana* stigmas resulted in a *fer*-like phenotype that correlates with sequence divergence in the extracellular domain of FER. Our findings show that the female control of pollen tube reception is based on a *FER*-dependent signaling pathway, which may play a role in reproductive isolation barriers.

In contrast to animals, where the products of meiosis differentiate directly into gametes, the meiotic products of higher plants undergo further mitotic divisions to form multicellular haploid structures called gametophytes, which in turn produce the gametes. To accomplish fertilization, the gametophytes communicate with and recognize each other. In angiosperms, the male gametophyte (pollen) germinates on the stigma and the growing pollen tube delivers the two nonmotile sperm cells to the female gametophyte (embryo sac). Proper delivery depends on signals from the female gametophyte (*1*, *2*). These chemotactic signals guide the pollen tube into the micropylar opening of the ovule, the reproductive structure that harbors the female gametophyte. In the majority of flowering plants, including *Arabidopsis thaliana* (Brassicaceae), the female gametophyte consists of seven cells: the egg cell, the two synergids (which lie just inside the micropylar opening of the ovule), the central cell, and the three antipodals (*3*) (Fig. 1A). In *Torenia fournieri* (Scrophulariaceae), the two synergids are necessary for pollen tube guidance (*4*). In most species, one of the synergids degenerates prior to or coincident with the pollen tube approaching the micropyle (*5*). The pollen tube grows into the degenerating synergid through the filiform apparatus, a structure formed by invaginations of the cell wall of

---

[1] Institute of Plant Biology and Zürich-Basel Plant Science Center, University of Zürich, Zollikerstrasse 107, CH-8008 Zürich, Switzerland. [2] Key Laboratory of Molecular and Developmental Biology, Institute of Genetics and Developmental Biology, Chinese Academy of Sciences, Beijing 100101, China.

*To whom correspondence should be addressed. E-mail: grossnik@botinst.uzh.ch